Monitoring and Mapping of fast and slow subsidence in hard rock metal mining using SAR Interferometry Techniques on high resolution TSX/TDX Satellite Data

Avinash Singh[1], Mohammad Soyeb Alam[1], Mohammad Khalid Umar[1]
21mt0097@me.iitism.ac.in; msalam@iitism.ac.in; 24mt0250@iitism.ac.in
[1]Department of Mining Engineering, Indian Institute of Technology (Indian School of Mines), Dhanbad, India

Keywords: Mining, Deformation, Monitoring, TSX/TDX, DInSAR, PSI

Abstract

Mining induced deformation in underground metal mines poses a threat to surface infrastructure, underground access and environmental safety, and needs reliable spatially continuous monitoring. In this contribution, a long-term interferometric SAR analysis over an underground hard rock metal mine (Mine-B) in Khetri Copper Belt, India using TSX/TDX high resolution SAR data is carried out. Coherent small baseline DInSAR time series (CSB-DTS), stacking DInSAR, and single reference PSI chain are implemented. Stacking DInSAR derived average LOS deformation velocity and single-reference PSI derived velocity are obtained for mine-B for dataset of January 2023- December 2024. The obtained results verify that Mine-B is substantially stable while having a persistent fast and slow deformation concentrated inside and around the trough in SoZ-2 in Mine-B. The workflow shows how the combination of CSB-DTS, stacked DInSAR and PSI can facilitate the operational subsidence monitoring and long-term stability evaluation in complex mining environments and gives an indication for the future integration with in-situ measurements and numerical models.

1. Introduction

Land surface deformation refers to measurable changes in the Earth's surface from its original position, expressed as either sideways shifting or vertical movement in the form of sinking (subsidence) or rising (uplift). Zhao and Zhu (2020) demonstrate that such changes are driven by both natural processes and human activities. Natural causes include the slow pressing down of loose sediments, melting of frozen ground in cold regions, dissolving of limestone and similar rocks, and movements of the Earth's crust. Although these processes usually occur slowly, they can still reshape landscapes and disturb water systems and ecosystems. Human actions, by contrast, often produce quicker and more severe changes. Soliman (1998) shows that pumping out groundwater, extracting oil and gas, using geothermal energy, large-scale construction, and especially underground mining are leading causes of subsidence. Kratzsch (1983) explains that Mining-induced subsidence happens when underground material is removed and the rocks above lose support, leading them to bend, crack, or collapse into empty spaces.

This movement shows up on the surface as hollows, cracks, scarps, or bowl-shaped depressions. Hartman (1992) and Clayton et al. (2018) reported that subsidence may occur suddenly after a roof or pillar fails, or slowly over years as stresses continue to shift. Its consequences are serious, it can damage buildings, roads, and pipelines, disrupt transport, change groundwater flow, cause flooding or waterlogging, reduce farm yields, and harm the environment. Although it is often considered an unavoidable result of underground mining, better prediction and monitoring can reduce its impacts as reported by Hartman (1992). Gili et al. (2000) in their report indicated that conventional monitoring techniques like precise levelling and GNSS networks can provide millimetric accuracy but are intensive in terms of labour, expensive and are usually restricted to sparse benchmarks which restricts them in their ability to represent full fields of deformation over large or inaccessible mining areas. Massonnet and Feigl (1998) and Rosen et al. (2000) demonstrate the complementary nature of space-borne Synthetic Aperture Radar interferometry (InSAR) for spatially contiguous measurement of line-of-sight (LOS) ground deformation, which is largely independent of illumination and weather conditions. Raucoules et al. (2007) further showed that SAR interferometry is effective for detecting and assessing ground subsidence, while Herrera et al. (2007) demonstrated the usefulness of advanced DInSAR analysis for monitoring deformation in mining areas. Ferretti et al. (2001) and Berardino et al. (2002) show that time-series InSAR techniques, such as Persistent Scatterer Interferometry (PSI) and Small Baseline Subset (SBAS), can reduce the effects of the atmospheric and orbital artefacts; and Crosetto et al. (2016) review the maturity of PSI for operational deformation monitoring. Wempen and McCarter (2017) show how high-resolution X-band SAR missions such as TerraSAR-X and TanDEM-X with short revisit times and metre-scale spatial resolution can allow detailed mapping of the gradients and small-scale mechanics of deformation patterns in complex mine environments. For the present hard-rock underground metal mine complex, Alam et al. (2022) by using an integrated DInSAR-PSI approach using TerraSAR-X/TanDEM-X data to characterise mining induced deformation and demonstrate the benefits of where distributed and point-wise deformation measurements can be combined in an underground mining environment.

Building on this earlier work, the present study exploits a new TerraSAR-X/TanDEM-X (TSX/TDX) StripMap data set acquired between January 2023 and December 2024. The objective of this study is to derive coherent small baseline DInSAR (CSB-DTS) deformation time series for Mine-B to estimate average deformation velocities using stacking DInSAR, retrieve PS-based deformation velocities for persistent scatterers, and interpret the long term deformation behaviour of the mining by combining these results with existing geological and mining condition related with mine safety and statute requirements.

2. Study Area and Data

2.1 Geographical Location of Study Area

The current area that is being investigated is located in the Khetri Copper Belt (KCB), which is one of the copper-rich belts, which is located in India. The study area includes underground hard rock metal mines utilizing mine lease boundaries, designated as Mine-B. The geographical location of the study area is latitude N 28°00'46" to N 28°05'50" and longitude E 75°45'32" to E 75°49'53”. The mine uses underground stoping methods and forms stoped-out zones (SoZs) at depth. At surface, there is plant facility, waste dump, haul road and townships and land covered with forest and cultivated land. Our current study area is Mine-B as shown in figure 1.

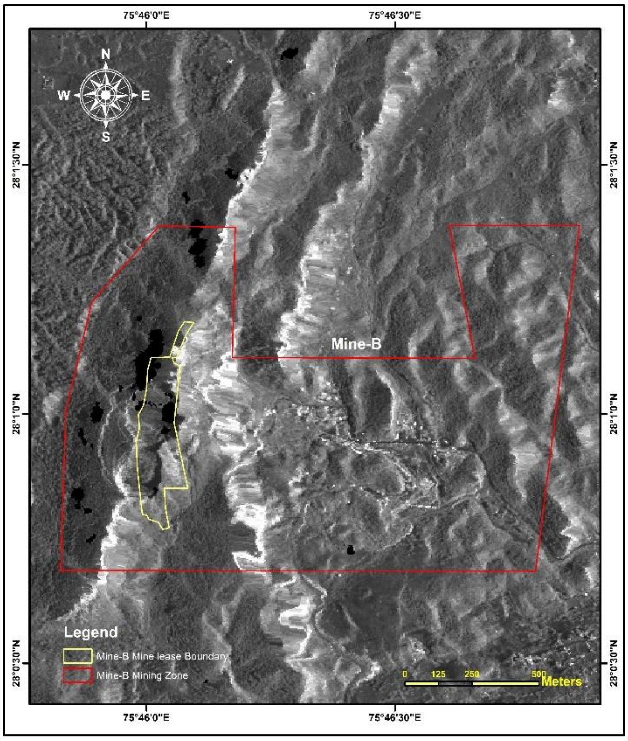

Figure 1. Geographic Location of the application area (Mine-B), KCB, India as shown in multi-look intensity SAR image

2.2 Satellite Data and Field Data

Cartosat-1 stereo pair data sets were acquired from Cartosat-1, which is a unique stereoscopic satellite mission with the capacity of acquiring along-track stereo images with a fixed B/H ratio. Basic information of Cartosat-1 stereo pair data sets used for DEM generation.

A stack of time-series InSAR data sets was acquired from TerraSAR-X (TSX-1) and TanDEM-X (TDX-1) satellite missions. TSX-1 and TDX-1 are commercial German Synthetic Aperture Radar (SAR) Earth Observation (EO) satellites launched in June 2007 and June 2010, respectively.

Ground Control Points (GCPs) covering the entire study area were acquired using dual-frequency GNSS receivers (Leica GS12 and GS16) operating in static relative positioning mode to support the generation and validation of the Cartosat-1 DEM. After post-processing, precise global coordinates of the GCPs expressed in WGS 1984 UTM Zone 43 (E, N, and ellipsoidal height) were obtained for use in both the DEM creation and its accuracy assessment.

Ground Control Points (GCPs) for the mine lease boundary of Mine-B were acquired using dual-frequency GNSS receivers operated in static relative positioning mode. This approach provided highly accurate global coordinates for the mine lease boundaries, which were then used to digitize the underground working plans in a global coordinate system along with other essential and relevant plans.

Satellite pair	InSAR pairs acquisition dates	B⊥ (m)	Bt (day)	$BfDC$ (Hz)	InSAR pairs number
TDX1-TDX1	Jan 03,2023-Feb 05,2023	-175.59	33	-101.31	1-2
TDX1-TDX1	Feb 05,2023-Mar 10,2023	309.23	33	47.16	2-3
TDX1-TDX1	Mar 10,2023-Apr 12,2023	54.52	33	-11.59	3-4
TDX1-TSX1	Apr 12,2023-May 15,2023	335.35	33	-40.85	4-5
TSX1-TDX1	May 15,2023-June 17,2023	-324.25	33	87.81	5-6
TDX1-TDX1	Oct 27,2023-Nov 29,2023	-138.80	33	9.11	10-11
TDX1-TSX1	Nov 29,2023-Jan 01,2024	298.92	33	-24.57	11-12
TSX1-TSX1	Jan 01,2024-Feb 03,2024	-174.10	33	-59.67	12-13
TSX1-TSX1	Feb 03,2024-Mar 07,2024	152.58	33	44.96	13-14
TSX1-TSX1	Mar 07,2024-Apr 09,2024	-30.23	33	-56.02	14-15
TSX1-TSX1	Apr 09,2024-June 14,2024	-88.86	66	82.50	15-16
TSX1-TSX1	Oct 13,2024-Oct 24,2024	81.79	11	27.19	18-19
TSX1-TDX1	Oct 24,2024-Dec 07,2024	-278.44	44	-37.58	19-20
TDX1-TSX1	Dec 07,2024-Dec 29,2024	354.13	22	3.69	20-21

Table 1. Baseline configuration of time series interferometric pairs of CSB-DTS

Satellite	**Acquisition dates**	**B⊥ (m)**	**Bt (days)**	**$BfDC$ (HZ)**	**#**
TDX1	Jan 03,2023	-185	-330	-33.184	1
TDX1	Feb 02,2023	-360	-297	68.129	2
TDX1	Mar 10,2023	-51	-264	20.969	3
TDX1	April 12,2023	3	-231	32.565	4
TSX1	May 15,2023	339	-198	73.415	5
TDX1	June 17,2023	14	-165	-14.394	6
TSX1	July 20,2023	256	-132	10.015	7
TDX1	Aug 22,2023	-67	-99	20.235	8
TSX1	Sept 24,2023	240	-66	47.586	9
TDX1	Oct 27,2023	139	-33	10.016	10
TDX1	Nov 29,2023	0	0	0	11
TSX1	Jan 01,2024	299	33	24.579	12
TSX1	Feb 03,2024	125	66	84.249	13
TSX1	Mar 07,2024	277	99	54.544	14
TSX1	April 09,2024	247	132	110.570	15
TSX1	June 14,2024	158	198	28.066	16
TDX1	Sep 10,2024	22	286	-8.319	17
TSX1	Oct 13,2024	160	319	57.611	18
TSX1	Oct 24,2024	242	330	0.867	19

TDX1	Dec 07,2024	-37	374	38.449	20
TSX1	Dec 29,2024	317	396	34.757	21

Table 2. Baseline configuration of TSX-1 and TDX-1 InSAR pairs (Orbit phase 1, Rel. Orbit 75, Beam spot_057R) using single reference (Scene # 11, dated Nov 29, 2023)

3. Methodology

The general methodological process included five major steps - selection and pre-processing of TerraSAR-X/TanDEM-X StripMap SAR scenes, generation and validation of a high resolution Cartosat-1 DEM, CSB-DTS based interferometric processing, stacking DInSAR for average LOS deformation velocity estimation and Single-Reference PSI processing for monitoring slow deformation over persistent scatterers. The complete workflow is summarised in Figure 2.

In the case of interferometric analysis, SAR scene data obtained between January 2023 and December 2024 was filtered on the basis of temporal baseline, perpendicular base as well as Doppler properties so as to maintain consistency and reduce geometric decorrelation. All the scenes were checked for layover and shadow effects, co-registered to the same geometry, and re-sampled for further interferometric processing. A high-resolution DEM produced from stereo data of the Cartosat-1 satellite using GNSS based ground control points was used for terrain geocoding, spatial referencing of the products of deformation and elimination of the topographic phase contribution. This was particularly important due to the nature of the mine area with rugged relief, steep slopes and mining-induced terrain disturbance can have a significant effect on interferometric reliability.

Thereafter, from the coherent small baseline DInSAR time-series (CSB-DTS), filtered and unwrapped differential interferograms were used to generate the stacking DInSAR for average LOS deformation velocity and the zones of relatively rapid deformation. In support of this, a single-reference PSI workflow on IPTA processing was applied to estimate point-wise LOS deformation velocities on coherent persistent scatterers, thus allowing detailed identification of slow and localized deformation. Lastly, the results of both methods were combined with stoped-out zone borders, map of mine layout, and field data to differentiate stable and deforming places, especially the ones of SoZ-2, and to help assess long-term mine stability.

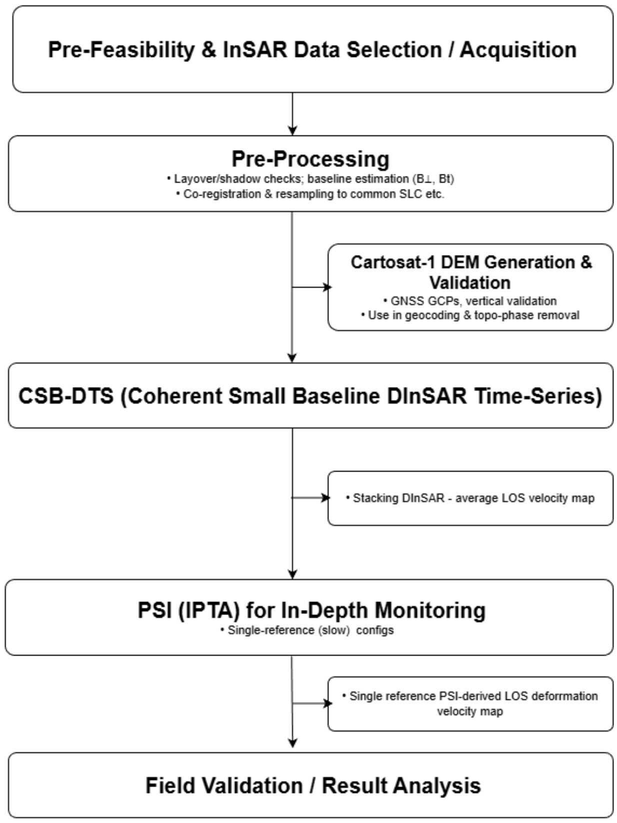

Figure 2. Flow diagram of formulated research methodology

4. Results and Discussion

4.1 Cartosat-1 DEM Generation and Validation

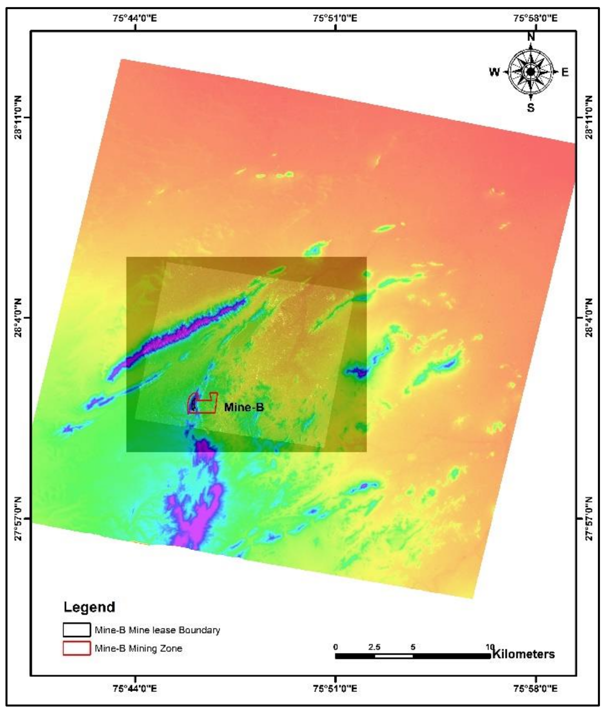

Figure 3. The high resolution generated and validated Cartosat-1 DEM using GCPs collected from GNSS receiver; superimposed on mining zones, mine lease boundaries and TSX- 1/TDX-1 MLI SAR image.

DEMs (relative and absolute) were computed based on high-resolution Cartosat-1 stereo pair data sets (received by IRS) and GCPs obtained by using dual-frequency GNSS receiver, without GCPs and GCPs obtained with the assistance of Google Earth. Further, DEMs were checked by test points and then, RMS error of various generated DEMs and SRTM DEM was calculated and compared. The known RMS error of vertical accuracies has been observed to range at 2.54 m with Cartosat-1 DEM produced with collected from dual-frequency GNSS receiver. Figure 3 depicts the high resolution produced and validated Cartosat-1 DEM with the help of GCPs obtained with the dual-frequency GNSS receiver. To get more information about the received results of Cartosat-1 DEM Generation and Validation, see the publication of the author Alam et al. (2018).

4.2 Stacking DInSAR Derived Average LOS Deformation Velocity

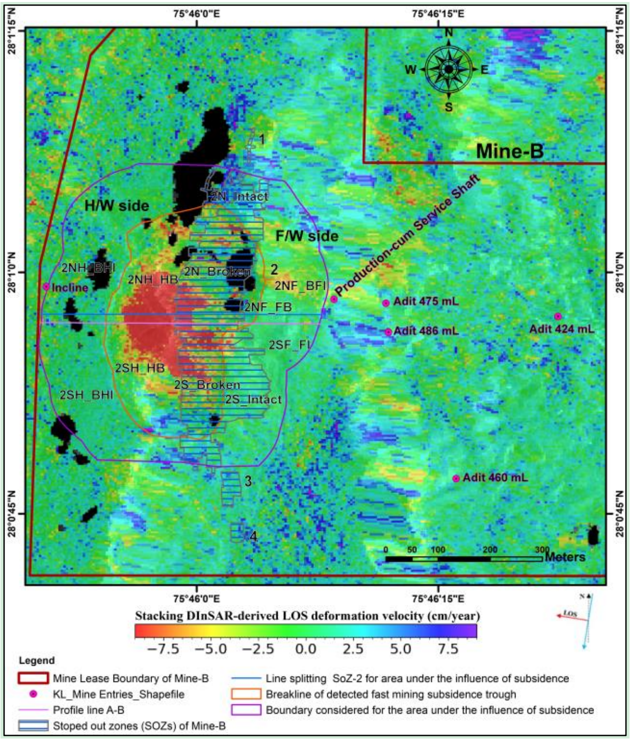

Figure 4. Stacking DInSAR-derived average LOS deformation velocity map over the study area (Mine-B). This result is superimposed on the average multi-look intensity image of TSX-1/TDX-1 data sets. The black hatched polygons illustrate the stoped-out zones (SoZs) mapped with the underground level plans updated until the observation period.

In order to obtain the average LOS deformation velocity over the Mine-B area, the stacking DInSAR of satellite data as shown in Table 1 was implemented over the unwrapped filtered differential interferograms that was obtained from the CSB-DTS processing. The resulting average LOS deformation velocity reflects deformation rate based on multiple interferometric pairs, sampled during different times, which represent both linear and non-linear behaviour during the observation period while further suppress the effect of atmospheric artefacts. Figure 4 gives the average LOS deformation velocity maps for Mine-B.

In Mine-B (Figure 4), no significant average LOS deformation velocity is noticed inside or outside most of the stoped-out zones. The obvious exception to this is the set of blocks associated with SoZ-2 i.e., that collapsed surface blocks and those located between the hanging wall/footwall contact and the SoZ-2 breakline, in which distinct fast subsidence signals are detected. The correlation between the stoped-out zones (inside and outside) and the measured average LOS deformation velocity was discussed by performing quantitative statistical analysis (Table 3 for inside SoZs and Table 4 for outside SoZs), which was separately computed for each stoped-out zone.

These statistics confirm again that generally significant fast subsidence is not present inside and outside of the stoped-out zones except in and around SoZ-2, particularly in blocks 2N_Broken, 2S_Broken, 2NH_HB and 2SH_HB, where clear fast subsidence signals are observed. Therefore, there is a need to apply higher accuracy DInSAR methods in order to address slow as well as fast subsidence signals inside and outside SoZs of the Mine-B area, particularly where CSB-DTS could not reveal the slow as well as fast subsidence signals.

Statistical results illustrate relatively noticeable fast subsidence signals in blocks 2N_Broken, 2S_Broken, 2NH_HB, and 2SH_HB, with average-LOS deformation velocity (mean ± std.dev) of -21.6±18.7 mm/yr, -27.3±19.5 mm/yr, -30.4±22.7 mm/yr, and -27.7±27.7 mm/yr respectively. In addition to this, maximum average LOS deformation velocity of -68.1 mm/yr, -78.4 mm/yr, -95.8 mm/yr, and -105.2 mm/yr observed in 2N_Broken, 2S_Broken, intact and coherent part of 2NH_HB, and 2SH_HB. The fast-subsiding blocks could not be validated with the aid of GNSS observations, as these areas are mistakenly found within the breakline of the detected subsidence trough and could not be readily accessed. To further study the spatial gradient of average LOS deformation velocity in the zone of Fast deformation, a spatial profile was extracted along line A-B (across-strike) using results of the stacking-DInSAR average LOS velocity. The corresponding profile is given in Figure 5.

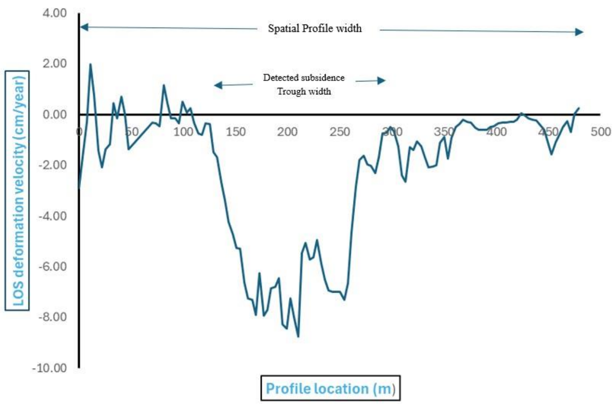

Figure 5. Spatial profile of average-LOS deformation velocity over the area

statistics inside SoZs			Stacking DInSAR (January 03,2023-December 29, 2024)				
SoZ no.	Description of blocks inside SoZs	Area* (km²)	Average LOS deformation velocity value (mm/year)				Remarks
			Min	Max	Mean	Std dev.	
1	Intact surface	0.0004	-24.2	21.5	-1.7	13.1	Slow as well as fast subsidence signals may exist
	2N_Intact	0.0071	-46.0	33.0	2.3	13.0	

https://doi.org/10.5194/isprs-archives-XLIX-B3-2026-529-2026

2	2N_Broken	0.0213	-68.1	32.4	-21.6	18.7	Fast subsidence signals Observed, slow subsidence signals may also exist
	2S_Intact	0.0148	-54.6	32.4	-6	9.7	Slow as well as fast subsidence signals may exist
	2S_Broken	0.0153	-78.4	22.3	-27.3	19.5	Fast subsidence signals observed, slow subsidence signals may also exist
3	Intact surface	0.0018	-25	16.3	1	6.8	Slow as well as fast subsidence signals may exist
4	Intact surface	0.0008	-22.6	24.9	1.5	10.1	

Table 3. Statistics of average LOS deformation velocities derived by stacking DInSAR inside each stoped out zone (SoZ) of the Mine-B

Note: (1) 2N_Intact (Intact surface in northern part); 2N_Broken (Broken/Collapsed surface in northern part); 2S_Intact (Intact surface in southern part); 2S_Broken (Broken/Collapsed surface in southern part) inside SoZ-2. **(2a)** *the areas of stoped-out zones were calculated from the underground working-level plans update till the observation period. **(2b)** the negative sign of the deformation velocity stands for an increasing distance with time away from the satellite, i.e., subsidence, whereas the positive sign shows a decreasing distance with time away from the satellite, i.e., uplift. **(2c)** Sub-millimeter level in Tables 3 and Table 4 is only the results of statistical computing, not representing that the deformation measured on a sub- millimeter level.

Statistics outside Stoped-out zones (SoZs)		Stacking DInSAR (January 03, 2023-December 29, 2024)					
SoZ no.	Description of blocks outside SoZs	Area (km²)	Average LOS deformation velocity value (mm/year)				Remarks
			Min.	Max.	Mean	Std. dev.	
1	Intact surface in both H/W and F/W side	-	-	-	-	-	Statistics outside SoZs not considered
2	2NH_HB	0.0219	-95.8	14.8	-30.4	22.7	Fast subsidence signals observed, slow subsidence signals may also exist
	2NH_BHI	0.0427	-42.3	29.5	3.5	8.8	Slow as well as fast subsidence signals may exist
	2NF_FB	0.0027	-95.8	14.8	-30.0	22.7	Slow as well as fast subsidence signals may exist
	2NF_BFI	0.0263	-42.5	36.4	-8.7	12.3	Fast subsidence signals observed, may be issue of phase ambiguity, slow subsidence signals may also exist
	2SH_HB	0.0222	-105.2	38.6	-27.7	27.7	Fast subsidence signals observed, slow subsidence signals may also exist
	2SH_BHI	0.0374	-37.6	31.5	2.4	8.2	Slow as well as fast subsidence signals may exist
	2SF_FI	0.0219	-28.9	25.7	3.6	5.6	
3	Intact surface in both H/W and F/W side	-	-	-	-	-	Statistics outside SoZs not considered
4	Intact surface in both H/W and F/W side	-	-	-	-	-	

Table 4. Statistics of average LOS deformation velocities derived by stacking DInSAR outside SoZ-2 of the Mine-B

Note: 2NH_HB (Collapsed and intact surface in between H/W contact and breakline in northern part); 2NH_BHI (Intact surface in between breakline, H/W contact, and boundary considered for the area under the influence of subsidence in northern part); 2NF_FB (Collapsed surface in between F/W contact and breakline in northern part); 2NF_BFI (Intact surface in between breakline, F/W contact and boundary considered for the area under the influence of subsidence in northern part); 2SH_HB (Collapsed and intact surface in between H/W contact and breakline in southern part); 2SH_BHI (Intact surface in between breakline, H/W contact and boundary considered for the area under the influence of subsidence in southern part); 2SF_FI (Intact surface in between F/W contact and and boundary considered for the area under the influence of subsidence in southern part) outside SoZ-2.

4.3 Results of Single Reference PSI-derived LOS Deformation Velocity

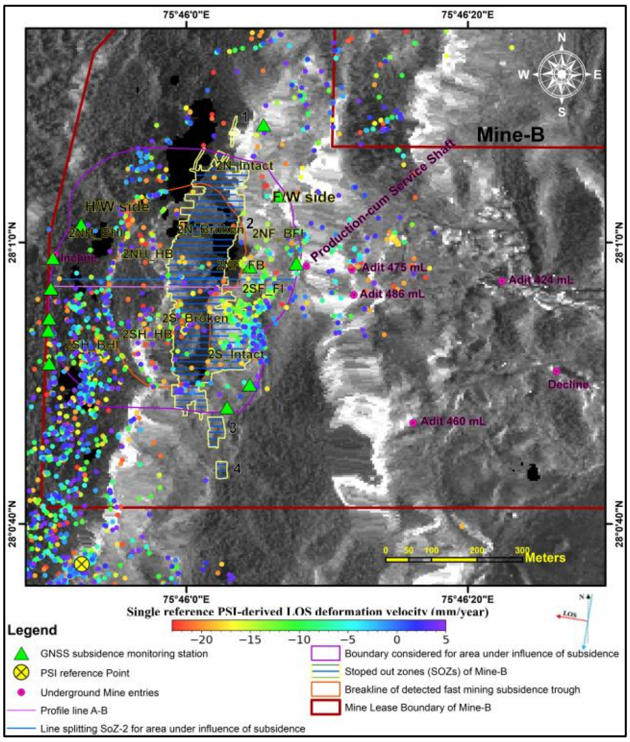

Figure 6. Single reference PSI-derived estimated LOS deformation velocity map over the study area (Mine-B) between January 03, 2023-December 29, 2024.

The data used for IPTA processing is shown in Table 2 with reference scene 11. The locations and the estimated LOS deformation velocities of the PSCs detected by single reference IPTA at Mine-B of the study area are shown in Figure 6. It also shows the PSI reference point that can be used to estimate PSC deformation velocities in Mine-B, which falls in a stable area, and is not within the mining territory. Moreover, the GNSS subsidence monitoring stations, which are used to confirm the PSI results, along with their corresponding GNSS reference stations have been indicated in the same figure. The negative deformation velocities are traditionally used to refer to a distance between the ground and the satellite that increases with time (i.e. subsidence) whereas the positive ones represent a decreasing distance with time (e.g. uplift). Figure 6 indicates that the significant amount of final PSCs can be obtained within the study window 4.2 km × 4.1 km that includes Mine-B. The majority of these PSCs are boulders and point like outcrops on ridges and hillslopes, and some man-made structures and medium-sized waste-rock boulders created during underground mining. There is a subgroup of PSCs that is linked to coherent distributed targets and they are primarily flat rock surfaces or rock surfaces, which are partially covered by soil on the hills slopes.

The PSCs are unevenly distributed spatially within and outside single stoped-out zones (SoZs). There are very little or no PSCs within and on SoZ -1, SoZ -3 and SoZ -4 (no PSCs at all), and block 2N-Intact, 2N-Broken, 2NF-FB. The density of PSCs within and outside SoZs, including 2S_Broken, 2NF_BFI, 2NH_HB and 2SH_HB has been observed to be moderate, but relatively high PSC density is detected in and around 2S_Intact, 2SF_FI, 2NH_BHI and 2SH_BHI. The low PSC densities are predominantly linked to blocks characterized by high deforming collapsed or broken surfaces, collapsed and partially intact ground, non-linear motion which is strongly non-linear or sparsely vegetated soils on the hill slopes. Moderate PSC coverages are those found in situations of the so-called mixed scatterer conditions such as bare point-like rocky surfaces, boulders, flat or gently sloping, part covered by soil rock, rock-soil mixtures with relatively denser vegetation, sparsely covered soil, and relatively slow moving collapsed or intact soil. Dense PSC layers are usually formed in areas where boulders and point-like rock outcrops are common to the ridges and the slope, flat or gently sloping rock surfaces which are sometimes so covered by soil.

Generally, the field of single-reference PSI-calculated deformation velocity of the Mine-B condition shows that the majority of the territory is rather stable with LOS velocities ranging around -3 to 3 mm/year. Localised slow LOS deformation is identified both within and without some SoZs. Statistical analysis of the relationship between SoZs (inside and outside) and the LOS deformation velocities in terms of the number of final PSCs, mean and standard deviation of velocity (Tables 5 and 6 of inside and outside SoZs, respectively) is to quantify.

Statistical results show that significant slow subsidence signals mainly exist over block 2NF_BFI (outside SoZ-2), with LOS deformation velocities (mean±std.dev) of -2.67±4.39 mm/year, and maximum LOS deformation velocity of -15.9 mm/year. However, block 2NF_BFI suffers from moderate PSCs. The stability checking of 2NF_BFI is especially very important since one of the most important underground structures is the production-cum-service shaft (main mine entry) and all major level galleries are in and around this block. The existence of scattered stable PSCs around the production shaft is an indication that it is in a rather stable zone though a more concentrated PSC distribution would be desirable to develop a more detailed view of the subsidence behaviour as well as to enable study of any rapid deformation. Similar reasons are also important in Block 2SF_FI (on the footwall side outside SoZ-2). Statistical results reveal that 2SF_FI seems to be stable and correlated with a good density of PSC to be used as spatial interpretations, but its stability needs to be validated through the study of its potential fast deformations by using multi-reference PSI.

Further, slow subsidence signals also present in blocks 2N_Broken, 2S_Broken, 2NH_HB, and 2SH_HB with LOS deformation velocities (mean±std.dev.) of -4.34 ± 3.43 mm/year, -2.87 ± 4.64 mm/year, -3.51 ± 5.51 mm/year, -0.80 ± 3.33 mm/year and maximum LOS deformation velocities of -10.18 mm/year, -12.25mm/year, -17.27 mm/year, -20.44 mm/year, respectively The maximum LOS subsidence rates are -10.18 mm/year, -12.25 mm/year, -17.27 mm/year and -20.44 mm/year respectively. These blocks are however associated with low to moderate PSCs counts primarily owing to the problem of phase ambiguity with broken/collapsed ground, mixed broken/intact surfaces, and rapid deformation as it was pointed out by CSB-DTS and stacking DInSAR. Phase ambiguity may be alleviated in intact sectors through the utilization of multi-reference sequential processing of PSI.

Mine-B areas (SoZ-1, SoZ-3 and SoZ-4) do not have PSCs in and out of the area, hence there is no possibility of statistical analysis of these areas. The other two major blocks 2NHBHI and 2SHBHI (not a part of SoZ-2), now seem to be stable and are defined by the great quantity of PSCs that can be analysed spatially. However, stability of SoZ-3, SoZ-4, 2NH_BHI and 2SH_BHI must eventually be checked by subjecting multi-reference PSI to processing to study possible fast deformation that cannot be observed with the single-reference method.

Statistics inside stoped- out zones (SoZs)				Single reference PSI (January 03,2023-December 29, 2024)				
SoZ no.	Description of blocks inside SoZs	Area* (km²)	No. of PSCs	Estimated LOS deformation velocity value (mm/year)				Remarks
				Min.	Max	Mean	Std .dev	
1	Intact Surface	0.0004	-	-	-		-	No PSCs available
2	2N_Intact	0.0071	2	-5.34	-1.74	-3.54	2.54	Slow subsidence signal not observed Availability of low PSCs
	2N_Broken	0.0213	9	-10.18	0.96	-4.34	3.43	Slow subsidence signal observed Availability of low PSCs
	2S_Intact	0.0148	79	-10.44	3.55	-0.68	2.2	Slow subsidence signal observed Availability of high PSCs
	2S_Broken	0.0153	50	-12.25	4.38	-2.87	4.64	Slow subsidence signal observed Availability of high PSCs
3	Intact surface	0.0018	-	-	-	-	-	No PSCs available
4	Intact surface	0.0008	-	-	-	-	-	No PSCs available

Table 5. Statistics of estimated LOS deformation velocities derived by single reference PSI inside each stoped out zone (SoZ) of the Mine-B

Statistics outside stoped- out zones (SoZs)				Single reference PSI (January 03,2023-December 29, 2024)				
SoZ no.	Description of blocks outside SoZs	Area (km²)	No. of PSCs	LOS deformation velocity value (mm/year)				Remarks
				Min.	Max.	Mean	Std. dev.	
1	Intact Surface in both H/W and F/W side	-	-	-	-	-	-	Statistics outside SoZs not considered
2	2NH_HB	0.0219	51	-17.27	3.669	-3.51	5.51	Slow subsidence signal observed Availability of high PSCs
	2NH_BHI	0.0427	69	-1.84	1.45	0.19	1.12	Slow subsidence signal observed Availability of high PSCs
	2NF_BFI	0.0263	35	-15.9	2.27	-2.67	4.39	Slow subsidence signal observed Availability of moderate PSCs
	2SH_HB	0.0222	68	-20.44	4.91	-1.81	5.12	Slow subsidence signal observed Availability of moderate PSCs
	2SH_BHI	0.0374	226	-13.38	4.40	-0.80	3.33	Slow subsidence signal observed Availability of high PSCs
	2SF_FI	0.0219	191	-21.20	4.92	-0.38	2.38	Slow subsidence signal observed Availability of high PSCs
3	Intact surface in both H/W and F/W side	-	-	-	-	-	-	Statistics outside SoZs not considered
4	Intact surface in both H/W and F/W side	-	-	-	-	-	-	Statistics outside SoZs not considered

Table 6. Statistics of estimated LOS deformation velocities derived by single reference PSI outside SoZ-2 of the Mine-B

4.4 Limitations and Future Scope

Although the positive results of the suggested strategy are encouraging, certain limitations should be acknowledged. The PSI single-reference results can be affected by low to moderate density of PSC and potential phase ambiguity in the same blocks in regions of broken or mixed ground conditions, and in rapidly deforming sectors, can have poor interpretive quality. Moreover, some zones need additional validation since the present scatterer distribution cannot be used to examine the spatial analysis in detail. Multi-reference or sequential PSI processing along with other field-based validation in the targeted regions should therefore be incorporated in future work to enhance the solution to both rapid and localized deformation.

5. Conclusion

This paper introduces an InSAR-based approach for the monitoring of subsidence in underground mines with the combination of Coherent Small Baseline DInSAR (CSB-DTS), stacking DInSAR, and Persistent Scatterer Interferometry (PSI) with the high-resolution TSX/TDX data with shorter wavelengths. The approach can be used to effectively detect both rapid and gradual deformations in the mining areas. CSB-DTS detects sudden deformation events, stacking DInSAR gives information on long-term velocity trends, and PSI measures subtle and small-scale movements in stable scatterers.

The results from stacking DInSAR, derived average-LOS deformation velocity, show significant rapid subsidence mainly within the coherent regions around the trough where the maximum average-LOS deformation velocity of -105.2 mm/year is observed. Further spatial profiling along the line that is drawn over the stacking-DInSAR results reveals a similar deformation pattern as CSB-DTS, with the maximum average LOS deformation velocity reaching -8.76 cm/year in the coherent portion of the detected subsidence trough. Single reference PSI identifies a notable number of final Persistent Scatterers (PSCs) to spatially represent the signals of the deformation in Mine-B. However, both low and moderate PSCs are also observed within and outside some stoped out zones and excluding the collapsed and fast-moving blocks. The LOS deformation velocity results from the PSI show a generally stable pattern (±3 mm/year) for most of the study area except for some stoped-out zones in Mine-B, where significant slow subsidence signals are detected, which are not revealed by CSB-DTS and stacking DInSAR with maximum LOS deformation velocities of -21.20 mm/year in 2SF_FI zone, -20.44 mm/year in 2SH_HB zone, -17.27 mm/year in 2NH_HB zone and -12.25 mm/year in 2S_Broken zone. This integrated monitoring technique not only helps in detecting the subsidence but also gives important information about the stability of mining zones. It proposes the possibility of using the combination of satellite-based data, in-situ measurements and numerical models to ensure long term mine safety and environmental monitoring. Looking forward, the implementation of multi-reference PSI could improve the detection of fast subsidence, further increasing the accuracy of operational monitoring system in complex mining environment.

References

Alam, M.S., Kumar, D. and Upreti, V., 2018: Generation and validation of Cartosat-1 DEM for northern Aravali range of hillocks, Rajasthan, India. *Journal of Mines, Metals and Fuels*, 66(1), 48–54. doi.org/10.18311/jmmf/2018/27975.

Alam, M.S., Kumar, D. and Chatterjee, R.S., 2022. Improving the capability of integrated DInSAR and PSI approach for better detection, monitoring and analysis of land surface deformation in underground mining environment. *Geocarto International*, 37(12), pp.3607–3641. doi:10.1080/10106049.2020.1864028.

Berardino, P., Fornaro, G., Lanari, R. & Sansosti, E., 2002. A new algorithm for surface deformation monitoring based on small baseline differential SAR interferograms. *IEEE Transactions on Geoscience and Remote Sensing*, 40(11), pp.2375–2383. doi:10.1109/TGRS.2002.803792.

Clayton, M.A., Dugie, M., LeRiche, A., McKane, C. and Davies, A.G.L., 2018, October. Development of a monitoring network for surface subsidence at New Gold's New Afton block cave operation. In *Caving 2018: Proceedings of the Fourth International Symposium on Block and Sublevel Caving* (pp. 689-704). Australian Centre for Geomechanics. doi.org/10.36487/ACG_rep/1815_53_Clayton.

Crosetto, M., Monserrat, O., Cuevas-González, M., Devanthéry, N. & Crippa, B., 2016. Persistent Scatterer Interferometry: A review. *ISPRS Journal of Photogrammetry and Remote Sensing*, 115, pp.78–89. doi:10.1016/j.isprsjprs.2015.10.011.

Ferretti, A., Prati, C. & Rocca, F., 2001. Permanent scatterers in SAR interferometry. *IEEE Transactions on Geoscience and Remote Sensing*, 39(1), pp.8–20. doi:10.1109/36.898661.

Gili, J.A., Corominas, J. & Rius, J., 2000. Using Global Positioning System techniques in landslide monitoring. *Engineering Geology*, 55(3), pp.167–192. doi:10.1016/S0013-7952(99)00127-1.

Hartman, H.L. (ed.), 1992: SME Mining Engineering Handbook. 2nd ed. Society for Mining, Metallurgy, and Exploration, Littleton, Colorado.

Herrera, G., Mulas, J., Fernández, J., Tomás, R., Cooksley, G., Sánchez, M., Duro, J. & Arnáiz, A., 2007. Advanced DInSAR analysis on mining areas: La Unión case study, Murcia (SE Spain). *Engineering Geology*, 90(3–4), pp.148–159. doi: 10.1016/j.enggeo.2007.01.001.

Kratzsch, H., 1983: Mining Subsidence Engineering. Springer-Verlag, Berlin, Heidelberg. doi.org/10.1007/978-3-642-81923-0.

Massonnet, D. & Feigl, K.L., 1998. Radar interferometry and its application to changes in the Earth’s surface. *Reviews of Geophysics*, 36(4), pp.441–500. doi:10.1029/97RG03139.

Raucoules, D., Colesanti, C. & Carnec, C., 2007. Use of SAR interferometry for detecting and assessing ground subsidence. *Comptes Rendus Geoscience*, 339(5), pp.289–302. doi:10.1016/j.crte.2007.02.002.

Rosen, P.A., Hensley, S., Joughin, I.R., Li, F.K., Madsen, S.N., Rodriguez, E. & Goldstein, R.M., 2000. Synthetic aperture radar interferometry. *Proceedings of the IEEE*, 88(3), pp.333–382. doi:10.1109/5.838084.

Soliman, M.M., 1998. Environmental hydrogeology.

Wempen, M.J. & McCarter, M.K., 2017. Comparison of L-band and X-band differential interferometric synthetic aperture radar for mine subsidence monitoring in central Utah. *International Journal of Mining Science and Technology*, 27(1), pp.159–163.

Zhao, X. and Zhu, Q., 2020. Analysis of the surface subsidence induced by sublevel caving based on GPS monitoring and numerical simulation. *Natural Hazards*, *103*(3), pp.3063-3083. doi.org/10.1007/s11069-020-04119-0.